Optical diagnostics on the pre-chamber jet and main chamber ignition in the active pre-chamber combustion (PCC)

Qinglong Tang[a], Ramgopal Sampath[a,*], Manuel Echeverri Marquez[a], Priybrat Sharma[a], Ponnya Hlaing[a], Moez Ben Houidi[a], Emre Cenker[b], Junseok Chang[b], Gaetano Magnotti[a], Bengt Johansson[a]

[a] King Abdullah University of Science and Technology, Clean Combustion Research Center, Thuwal 23900, Saudi Arabia
[b] Transport Technology R&D, Saudi Aramco, Dhahran 31311, Saudi Arabia

ARTICLE INFO

ABSTRACT

We studied the relationship between pre-chamber jet and main chamber ignition in the pre-chamber combustion (PCC) of an optical engine, fueled with methane and equipped with an active pre-chamber with two rows of orifices. Acetone planar laser-induced fluorescence (PLIF) and OH* chemiluminescence imaging techniques were simultaneously applied to visualize the pre-chamber jet and the reaction zone in the main chamber, respectively. The pre-chamber fueling was constant and the main chamber fueling was increased to form an ultra-lean case and a lean case with global excess air ratios (λ) of 2.3 and 1.8, respectively. Results indicate that a higher pressure difference between pre-chamber and main chamber ($\triangle P$) produces larger pre-chamber jet penetration speed; the maximum pre-chamber jet penetration speed appears at timing around the peak $\triangle P$. Over enrichment of the pre-chamber charge reduces the peak $\triangle P$ and thus does not favor a faster pre-chamber jet discharge. In addition to the main pre-chamber jet, a weaker post jet discharge process is visualized; the former is due to the pre-chamber combustion while the latter due to the $\triangle P$ fluctuation and the cylinder volume expansion. The post pre-chamber jet is accompanied by a post reaction zone in the ultra-lean case (λ=2.3) and there are two unburned regions in the main chamber: one is around the pre-chamber nozzle and the other between the adjacent reaction zones. These two unburned regions are consumed by flame propagation in the lean case (λ=1.8). The weak pre-chamber jet from the upper-row orifice does not produce any distinct reaction zone, indicating that the pre-chamber orifice location and arrangement on the nozzle also matters in the pre-chamber design. The pre-chamber jet penetration length is longer than that of the reaction zone during pre-chamber discharge; the penetration length difference between the pre-chamber jet and reaction zone decreases with increasing main chamber fueling.

© 2021 The Combustion Institute. Published by Elsevier Inc. All rights reserved.

1. Introduction

Energy crises and environmental pollutions increase the demand for spark ignition (SI) engine efficiency improvement in the past decades. The ideal thermodynamic cycle of the SI engine, the Otto cycle, indicates that higher engine efficiency is achievable by increasing the compression ratio and specific heat ratio. Engine knock restricts a higher compression ratio of the SI engine. Therefore, lean combustion with a higher specific heat ratio was applied to boost engine efficiency. Lean combustion strategies can reduce pumping losses because of less throttling. It also reduces nitric oxide (NO_x) emissions due to the lower combustion temperature

which also lessens the heat transfer loss and further improves engine efficiency. However, the narrow flammability limits of most fuels lead to unstable combustion when the mixture is lean, which increases unburned hydrocarbons (UHC) and carbon monoxide (CO) emissions [1]. SI engine operated with a global excess air ratio (λ) higher than 1.4 will have unacceptable cycle-to-cycle variation [2]. The key to the next generation of the lean-combustion SI engine is to extend the lean limit while maintaining stable combustion.

The pre-chamber combustion (PCC) concept was proposed in the 1950s–1970s to meet lean-combustion challenges [3,4]. One successful example in this period was the Compound Vortex Controlled Combustion (CVCC) system developed by Honda in 1974 [5]. The pre-chamber is an extra small chamber apart from the cylinder (main chamber); it is equipped with a spark plug and

connected to the main chamber through several small orifices on the pre-chamber nozzle. The pre-chamber charge is introduced from the main chamber charge during compression stroke (passive pre-chamber) or by an auxiliary fuel supply line into the pre-chamber (active pre-chamber). Once the pre-chamber charge is ignited and pressure builds up, a chemically active turbulent pre-chamber jet is discharged into the main chamber. The idea of PCC is to use the pre-chamber as a generator of hot-radicals and turbulence to produce distributed ignition sites and faster main chamber combustion at a much leaner condition than the conventional SI engine [6,7]. In the last decade, the active pre-chamber has been extensively investigated to extend the lean limit of the PCC engine. Attard et al. [2] implemented an active pre-chamber on a light-duty gasoline SI engine with a compression ratio of 10.4; they extended the lean limit to $\lambda \sim 2$ with stable combustion and ultra-low NO_x emission. In further studies, they showed that the peak engine efficiency of PCC was 20% higher than the SI mode [8] and the peak net indicated thermal efficiency reached 42.8% [9]. Besides, the PCC engine also exhibited high knock tolerance [10] and robust ignition performance [11], which allowed a higher compression ratio. Shah et al. [12] modified a heavy-duty diesel engine for active PCC operation with a compression ratio of 12; a maximum gross indicated efficiency of 47.6% was achieved with the main chamber λ of 2.4. Their further studies indicated that larger pre-chamber volume and small pre-chamber orifices could extend the lean limit of main chamber combustion, however, at the expense of NO_x emission increase [13]. Hlaing et al. [14,15] designed a unique pre-chamber assembly with a long pre-chamber throat that could directly replace the injector of a heavy-duty diesel engine without further modification to the original cylinder head. They concluded that the indicated efficiency and emissions of PCC were largely determined by the global λ and the high gross indicated efficiency around 44% was observed between the global λ of 1.6 and 2.0; besides, a post-heat release stage was witnessed when the global charge is relatively rich ($\lambda = 1.3$).

Many optical diagnostic efforts explored the detailed flow and combustion physics of PCC in constant volume chambers (CVC) and rapid compression machines (RCM). Biswas et al. [16–18] investigated the ignition mechanism of PCC in a CVC using simultaneous high-speed Schlieren and OH* chemiluminescence imaging. They proposed two ignition mechanisms: jet ignition and flame ignition; the former showed flame quenching and produced a pre-chamber jet comprising of only hot combustion products, while the latter presented no flame quenching and the pre-chamber jet was comprised of turbulent flames and active radicals. Higher pressure and larger orifice diameter produce less flame quenching and thus result in the flame ignition mechanism. Regarding the effects of orifice diameter, Yamaguchi et al. [6] reported more detailed four scenarios (chemical chain ignition and well-dispersed burning; composite ignition and well-dispersed burning followed by wrinkled laminar burning; flame kernel torch ignition and wrinkled laminar burning; and flame front torch ignition and wrinkled laminar burning.) of the main chamber ignition process in an early CVC study. Mastorakos et al. [19] and Allison et al. [20] studied the flame propagation inside the pre-chamber and passing through the pre-chamber orifice in a CVC under atmospheric conditions; they schematically depicted the flame ignition and jet ignition mechanisms. Gentz et al. [21,22] investigated the pre-chamber orifice number and diameter design in an RCM extensively using the high-speed imaging technique. Gholamisheeri et al. [23,24] tried to quantify the flame penetration speed using high-speed imaging in an RCM and to link the pressure and ignition process to the two-dimensional simulation. However, the significantly different boundary conditions of these optical apparatus could not reproduce the practical PCC engine combustion. For example, the limited operating pressure of 1 to 5 bar in the

CVC studies [16–18] is much lower than that of the PCC engine conditions; this pressure difference may cause disparities in the practical PCC ignition mechanism. The RCM seems not suitable for the lean limit study of PCC that relies on the cycle-to-cycle variation analysis because it cannot be run continuously for many cycles. Meanwhile, the excessive heat loss from the pre-chamber assembly could cause a considerable impact on the main chamber combustion; one evidence is that the PCC could not extend the lean limit and the SI mode could even run much leaner than PCC in the RCM work [21]. Besides, the RCM does not have the intake and expansion process of engines; this could substantially affect the fuel/air charge distribution and the residual gas scavenging in pre-chamber, gas exchange between pre-chamber and main chamber, as well as emission formation from the pre-chamber.

Though line-of-sight, high-speed imaging of the PCC combustion process in optical engines gained useful insights. Kawabata et al. [25] applied high-speed imaging of the natural flame luminosity and found that increasing the number of the pre-chamber nozzle orifices could promote the ignition and combustion of lean mixture in the main chamber. Toulson [26] and Attard [27] investigated PCC and SI under the same optical engine using high-speed imaging; the flame probability distribution showed that PCC was faster and more stable at $\lambda=1.8$ compared to the SI mode at $\lambda=1.4$. Bunce et al. [28] evaluated the turbulent reaction zone of a PCC engine using high-speed imaging of OH* and CH* chemiluminescence; they found that the first visible reaction zones emerged around the peak of the pre-chamber pressure and speculated that a mass transfer from pre-chamber to main chamber existed between the pre-chamber pressure build-up and the first visible reaction zones. Duong et al. [29] tried to link the combustion images to the pre-chamber and main chamber heat release process and concluded that the variation in main chamber heat release did not correlate with the variations in pre-chamber. Korb et al. [30] investigated the charge motion and combustion of PCC by flame probability distribution analysis under different pre-chamber nozzle design; they asserted that the radial nozzle is better than the tilted nozzle in generating tumble flow for pre-chamber scavenging and thus favors faster flame torch discharge into the main chamber. Marquez et al. [31] compared the combustion characteristics of passive and active PCC using high-speed imaging; they found that the passive PCC mode (no direct fueling into the pre-chamber) exhibited a more random behavior in terms of the jet probability during the pre-chamber discharge.

To date, very few studies have applied laser diagnostics on optical engines to explore the detailed in-cylinder process of PCC. The first planar laser-induced fluorescence (PLIF) work on PCC was achieved by Wellander et al. [32], in which they studied the early flame development of PCC in the main chamber by only seeding the main chamber air with acetone tracer. The pre-chamber jet was visualized by the dark region in the PLIF field of view; this "negative" PLIF technique showed intense pre-chamber jet impingement on the piston wall. Most recently, Tang et al. [33] and Sampath et al. [34] applied simultaneous negative PLIF and OH* chemiluminescence imaging to investigate the gas exchange from the pre-chamber to the main chamber and the effects of pre-chamber enrichment on main chamber ignition, respectively. However, the relationship between the pre-chamber jet and the main chamber ignition region is still not well understood. The spatial distribution of the unburned regions of PCC has never been reported when the global λ is close to the lean limit. Meanwhile, the key factor that determines the pre-chamber jet penetration speed and the reason for the post-heat release stage reported in the literature [14] remain to be clarified.

In the present study, we investigated the active PCC in a heavy-duty optical engine equipped with a pre-chamber with two-row orifices. Simultaneous negative acetone PLIF and OH* chemilumi-
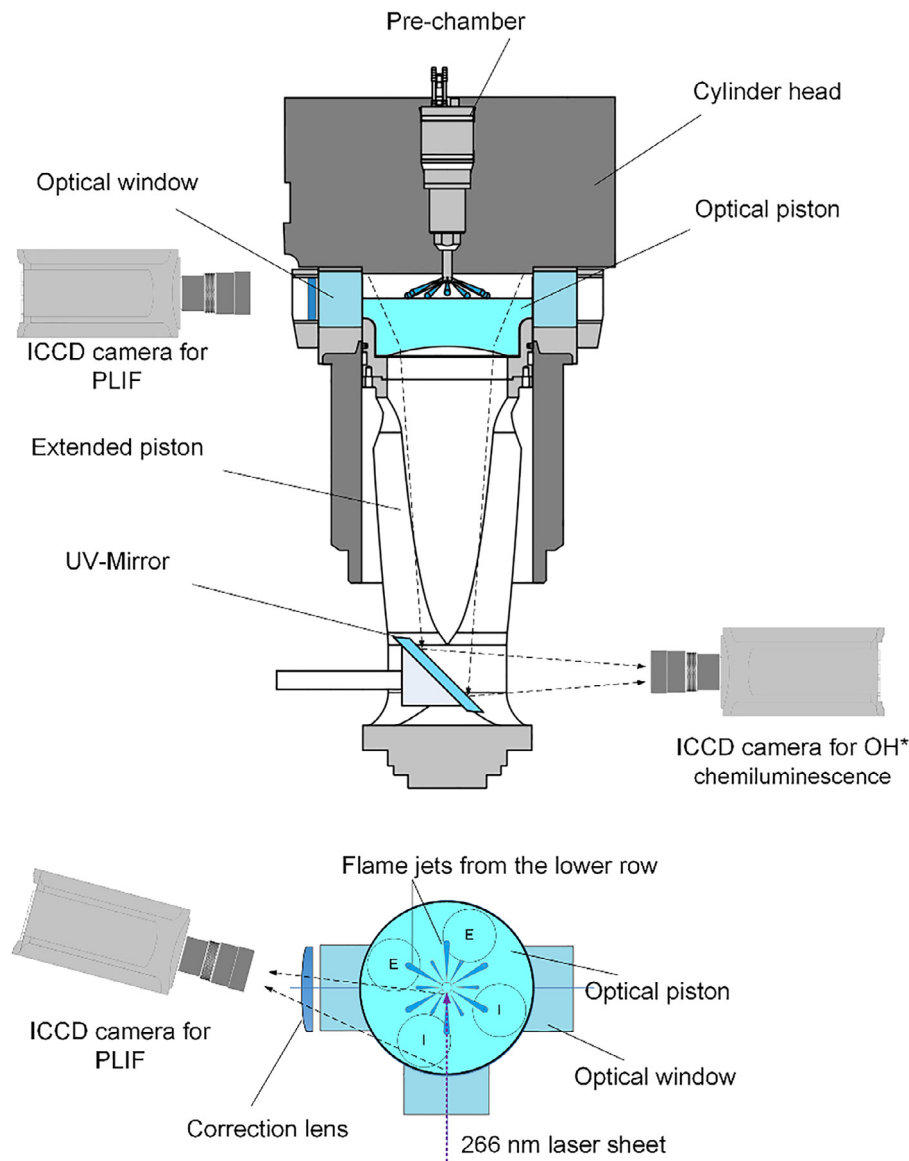
Fig. 1. Schematic of the optical engine and simultaneous PLIF (side view) and line-of-sight OH* chemiluminescence (bottom view) imaging system. The vertical laser sheet intersects one of the pre-chamber jets pointing to the side window.

nescence imaging were applied to visualize the pre-chamber jet and reaction zone, respectively. The objectives are: (1) to explore the relationship between the pre-chamber jet and main chamber ignition region by comparing the cases with and without main chamber fueling, (2) to evaluate the effects of global λ by keeping the pre-chamber fueling constant while increasing main chamber fueling, (3) to compare the pre-chamber jets discharged from the upper row and lower row orifices to highlight the importance of orifice location and arrangement in pre-chamber design, and (4) to clarify the spatial relationship between the pre-chamber jet and the reaction zone.

2. Experimental setup and optical diagnostic techniques

2.1. Optical engine and pre-chamber design

A four-stroke, heavy-duty optical engine equipped with a pre-chamber assembly was used in the experiment. One of the six cylinders was modified following the Bowditch design to allow for optical study while the others were deactivated. Figure 1

shows the schematic of the optical engine. It has an extended piston equipped with a flat optical piston crown. The cylinder is visible from the bottom view of the optical piston window when setting an aluminum-coated mirror below the extended piston. The piston-cylinder assembly is sealed with self-lubricating PTFE rings. Three quartz windows spaced 90° to each other on the side provide optical access for laser and camera imaging from the side view. The main optical engine specifications are listed in Table 1.

The structure of the pre-chamber assembly and some key dimensions of the pre-chamber body are shown in Fig. 2. More detailed information is provided in the previous works [14,15]. The pre-chamber assembly was designed to replace the original diesel injector of the optical engine without further modification to the cylinder head. The pre-chamber body is installed on an adaptor on which the spark plug, gas line, and pressure sensor (not shown in Fig. 2) are fixed. It features a narrow throat with an inner diameter of 3.3 mm and a length of 25 mm. Based on the recommendation of Gussak [7], the pre-chamber volume to cylinder clearance volume ratio was set to 2.5%, resulting in a pre-chamber volume of 5.07 cm^3. The nozzle area to pre-chamber volume ratio was
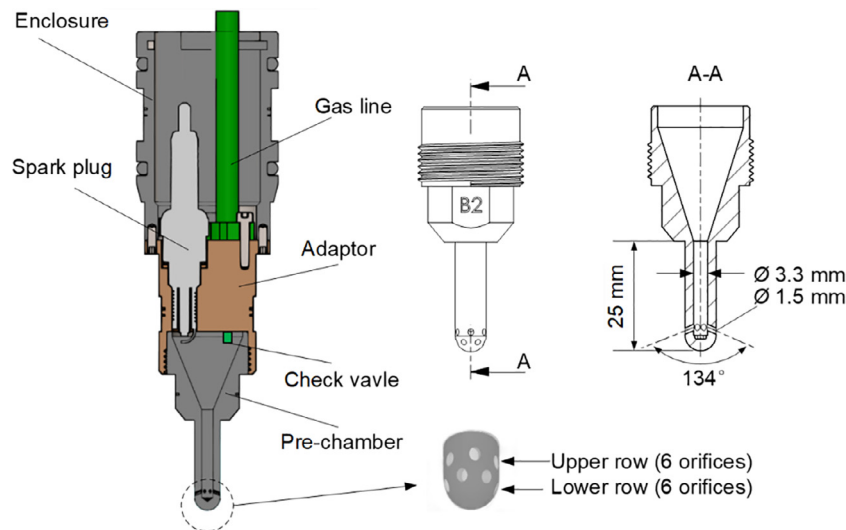
Fig. 2. Pre-chamber assembly and key dimensions of the pre-chamber body. An enlarged 3-D model of the pre-chamber nozzle shows the arrangement of two-row orifices.

Table 1
Optical engine specifications.

Bore	131 mm
Stroke	158 mm
Displacement	2.1 L
Connecting rod length	255 mm
Compression ratio	9.5
Combustion chamber shape	Flat
Intake valve open at	−330 °CA ATDC
Intake valve closed at	−170 °CA ATDC
Exhaust valve open at	180 °CA ATDC
Exhaust valve closed at	−340 °CA ATDC

Table 2
Engine operating conditions.

Engine speed	1200 rpm
Intake gas	Air
Spark timing	−15 °CA ATDC
Intake pressure	1.2 bar
Intake temperature	30 ± 1 °C
Coolant temperature	78 ± 2 °C
Oil temperature	88 ± 2 °C
Fuel	Methane (99.5% purity)
Pre-chamber and main chamber supply pressure	7 bar
Pre-chamber and main chamber injection timing	−360 °CA ATDC

Table 3
Test cases.

	Unfueled* case	Ultra-lean case	Lean case
Pre-chamber (PC) Fuel MEP (bar)	1.6	←	←
Main chamber (MC) Fuel MEP (bar)	0	12	16
PC fueling rate (mg/cycle)	7.2	←	←
MC fueling rate (mg/cycle)	0	54	72
PC fuel ratio	100%	11.8%	9.1%
Ratio of methane vol. per cycle to PC vol.	1.8	←	←
Global excess air ratio (λ)	**11.3**	**2.3**	**1.8**
Gross IMEP	−0.03	4.0	8.2
COV of IMEP	–	~12%	~3%
Gross indicated efficiency	–	26.2%	42.5%

* no fueling to the main chamber. ←: same as the other case.

set to 0.042 cm^{-1}. The narrow throat provides a limited area of the nozzle tip. Thus, two rows of nozzle orifices, six orifices per row, are arranged on the pre-chamber nozzle. The nozzle orifices are evenly spaced along the radial direction. The diameter of the nozzle orifices is 1.5 mm and the included angle for both rows is 134° The arrangement of the two-row orifices is shown in Fig. 2.

The pre-chamber has a separate methane supply line and the fuel flow rate is controlled by a mass flow meter and the injection timing by a gas block injector. The methane is supplied with 7 bar pressure and the injection timing is −360 °CA ATDC. The methane supply to the main chamber is delivered by two fuel injectors in the intake port with the same pressure and timing as the pre-chamber. The main chamber fuel flow rate is measured by another mass flow meter.

2.2. Operating conditions and test cases

The engine was run at 1200 revolutions per minute (rpm) during the experiment. The engine intake boosting and the pre-heating system kept the intake pressure and temperature at 1.2 bar and 30 °C, respectively. The intake air mass flow rate was measured by a mass flow meter. The spark timing was fixed at −15 °CA ATDC. To avoid optical windows overheating and fouling, the engine was run with a 10/5 skip fire mode in which 10 continuous fired cycles are followed by 5 motored cycles. Two piezoelectric pressure sensors (AVL GH15DK and Kistler 7061C) were installed in the pre-chamber and the main chamber to record the pre-chamber and main chamber pressure respectively during the experiment. Table 2 summarizes the main engine operating conditions.

There are three test cases in this study, as shown in Table 3. The pre-chamber fueling rate is kept at 7.2 mg/cycle and the main chamber fueling rate is increased from 0 to 54 and 72 mg/cycle. The fuel mean effective pressure (FuelMEP) is defined in Eq. (1), in which m, Q_{LHV}, and V_d are methane mass per cycle, methane low heat value, and cylinder displacement, respectively. The pre-chamber FuelMEP is 1.6 bar for all three cases. The main chamber FuelMEP for the three cases is 0, 12, and 16 bar, respectively. The calculated global excess air ratios (λ) of these three cases are 11.3, 2.3, and 1.8, respectively. For brevity, we denote these three cases as the unfueled case (PC7.2MC0), the ultra-lean case (PC7.2MC54), and the lean case (PC7.2MC72), respectively. In the abbreviation PC*x*MC*y*, x and y are the fueling rates in the pre-chamber and main chamber, respectively. The PLIF imaging of the jet from the lower-row orifice was carried out for all three cases, while the pre-chamber jet from the upper-row orifice was imaged only for the ultra-lean case. Table 4 summarizes the test matrix of the PLIF imaging of different orifices.

Table 4

PLIF imaging cases of the pre-chamber jets from different orifices.

	Unfueled case (PC7.2MC0)	Ultra-lean case (PC7.2MC54)	Lean case (PC7.2MC72)
Lower row orifice	√	√	√
Upper row orifice	×	√	×

"√": done. " × ": not done.

The heat release from the main chamber (Q_{MC}) and pre-chamber (Q_{PC}) is derived based on the first law of thermodynamics and considers the mass flow transfer (dm) between the two chambers [15,29]. The heat release rate in the main chamber ($dQ_{MC}/d\theta$) and pre-chamber ($dQ_{PC}/d\theta$) is expressed in Eq. (2) and (3), respectively. Since the pre-chamber volume is constant, the heat release term representing the volume change effect disappears in Eq. (3). The specific heat capacity (C_P) is evaluated based on the mixture of air and natural gas properties and bulk gas temperature of the charge. The dm is determined by the ratio of main chamber pressure (P_{MC}) and pre-chamber pressure (P_{PC}), where C_d is the discharge coefficient, A_T is the area of the nozzle holes, and R is the specific gas constant. More details about the heat release calculation can be found in [15] and [29]. The pressure and heat release rate data are averaged from 90 cycles.

$$\text{FuelMEP} = \frac{m \cdot Q_{LHV}}{V_d} \quad (1)$$

$$\frac{dQ_{MC}}{d\theta} = \frac{\gamma}{\gamma - 1} P_{MC} \frac{dV_{MC}}{d\theta} + \frac{1}{\gamma - 1} V_{MC} \frac{dP_{MC}}{d\theta} - C_P T_{PC,MC} \frac{dm}{d\theta} \quad (2)$$

$$\frac{dQ_{PC}}{d\theta} = \frac{1}{\gamma - 1} V_{PC} \frac{dP_{PC}}{d\theta} + C_P T_{PC,MC} \frac{dm}{d\theta} \quad (3)$$

$$dm = \frac{C_d A_T P_{PC}}{\sqrt{RT_{PC}}} \left(\frac{P_{MC}}{P_{PC}} \right)^{\frac{1}{\gamma}} \left[\frac{2\gamma}{\gamma - 1} \left(1 - \left(\frac{P_{MC}}{P_{PC}} \right)^{\frac{\gamma-1}{\gamma}} \right) \right]^{\frac{1}{\gamma}} \quad (4)$$

2.3. Negative fuel-tracer PLIF imaging of the jet from pre-chamber

Figure 1 shows the schematic diagram of the simultaneous negative PLIF and OH* chemiluminescence system. About 12 mg/cycle acetone was injected into the intake port with 4 bar pressure at −360 °CA ATDC to premix with air and served as the tracer of the main chamber charge. The fourth harmonic (266 nm, 27 mJ/pulse) of a 10 Hz Nd:YAG laser (Q-smart 850, Quantel) was used for the acetone excitation. The laser beam was formed into a vertical laser sheet less than 0.5 mm thick and 20 mm high by the laser sheet optics composed of three cylindrical lenses ($f_1 = -20$ mm, $f_2 = +100$ mm, and $f_3 = +1000$ mm).

An ICCD camera (PI-MAX3, Princeton Instruments), equipped with a Nikon 50 mm, f/1.2 visible lens, was placed on the left side of the quartz liner and was tilted to visualize the radial region from the pre-chamber to the cylinder wall. One convex cylindrical lens was installed on the left window to correct the camera focusing issue caused by the curvature of the side window. A tilt/shift lens mount adapter (Scheimpflug adapter) rotated the lens to a certain angle relative to the camera to correct the focus shift produced by the tilting of the ICCD camera. One low-pass filter (FF01–440/SP-25, Semrock) and one high-pass filter (BLP01–355R-25, Semrock) were combined to capture the acetone PLIF signal in the range of 355–440 nm. The gate width and gain level of the ICCD camera were 100 ns and 80%, respectively.

Note that acetone was only seeded into the main chamber by intake port injection while the pre-chamber remains unseeded. When no pre-chamber jet comes out from the pre-chamber, the field of view of the PLIF imaging in the main chamber would
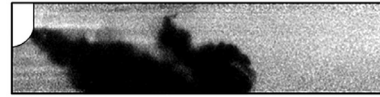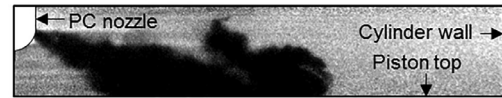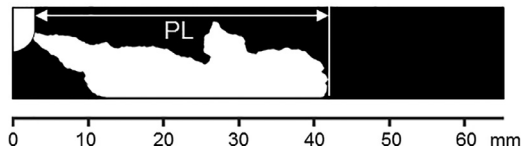

Fig. 3. Comparison between the negative PLIF images without (a) and with (b) window distortion correction. The pre-chamber (PC) nozzle, cylinder wall, and piston top wall are marked out. The image binarization is applied in (c) to detect the jet boundary and penetration length (PL).

be filled uniformly with the acetone fluorescence signal. It will show dark regions when the pre-chamber jet appears in the main chamber or flame consumes the acetone in the main chamber. Here, the reaction zone and pre-chamber jet in this study are defined as follows:

Reaction zone: the high-temperature flame region shown by the OH* chemiluminescence.

PC jet or jet: the gas jet shown by the negative PLIF region during the pre-chamber discharge. It contains the unseeded burned/unburned charge from the pre-chamber and the reaction region in the main chamber.

The pre-chamber jet region also contains the reaction zone based on the above definition, i.e., pre-chamber jet region ≥ reaction zone. The spatial relationship of the pre-chamber jet and the reaction zone will be discussed in Section 3.4. One example of the pre-chamber jet visualized by the negative PLIF is shown in Fig. 3.

The PLIF images are processed as follows: (1) the averaged background image was subtracted from the PLIF image; (2) the PLIF image was normalized by the image acquired at the same crank angle without pre-chamber combustion, which shows a uniform PLIF signal. This step removes the potential effects of laser sheet non-uniformity; (3) the distortion caused by the optical side window was corrected based on a grid-mapping technique using the piecewise linear dewarp algorithm in MATLAB. The same correction procedure was also used in our previous works [35,36].

Figure 3 presents an example of the negative PLIF image without and with distortion correction. The optical window produces a distinct image distortion, which would result in a big deviation to the estimation of pre-chamber jet penetration length. The locations of the pre-chamber nozzle, cylinder wall, and piston top are marked out. The pre-chamber jet boundary and the horizontal pre-chamber jet penetration length are determined after image binarization.

2.4. OH* chemiluminescence imaging

The other ICCD camera (PI-MAX3, Princeton Instruments) was used for line-of-sight OH* chemiluminescence imaging from the bottom view of the piston, as shown in Fig. 1. It was equipped with a 45 mm f/1.8 UV-lens (CERCO 2073, Sodern) and a bandpass filter with a transmission range of 300–330 nm, The OH* signal is an indicator of the high-temperature reaction zone. The gate
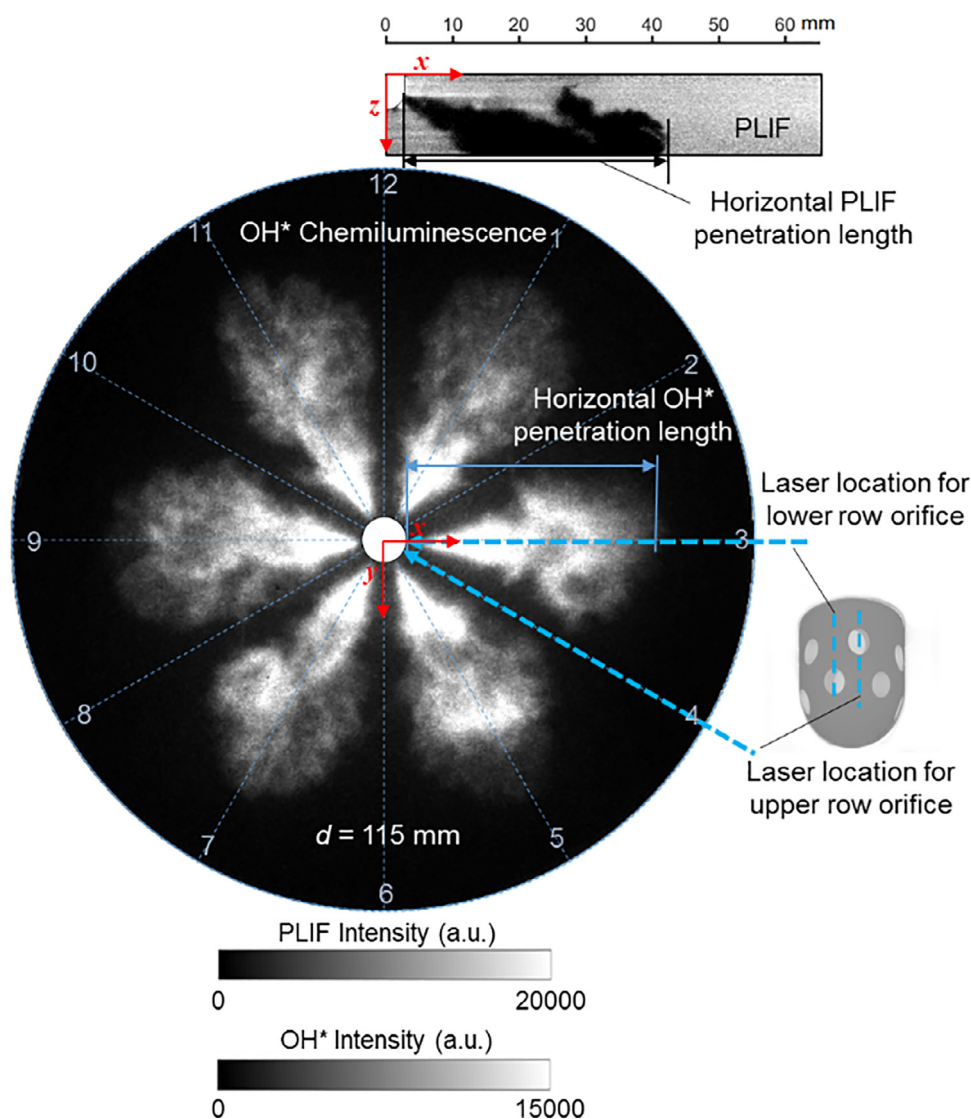
Fig. 4. An example of the simultaneously acquired single-shot negative PLIF image (lower row orifice) and OH* chemiluminescence image. The directions of the 12 orifices are labeled with numbers 1–12, in which the odd number and even number show the lower row and upper row orifices, respectively. The laser sheets for the lower row and upper row orifices are at the 3 and 4 o'clock directions, respectively.

width and gain level of the ICCD camera were 140 μs and 100%, respectively. These two cameras were synchronized in time and the gate of the OH* camera was 100 ns before the gate of the PLIF camera. Thus, the coupled images from PLIF and OH* are assumed synchronized and are considered to be at the same crank angle. Due to the low frequency of the laser, only one pair of PLIF and OH* images could be acquired from one engine cycle. Ninety PLIF/OH* image pairs were recorded during the experiment for each crank angle of interest.

The 2-dimensional correlation factors between each single-shot PLIF image and the average PLIF image were calculated to choose the "typical" single-shot PLIF image at specified crank angles. The single-shot PLIF image showing the highest correlation factor was selected as the typical single-shot image. Once the PLIF image was selected, the corresponding OH* image was obtained. Figure 4 shows a pair of single-shot PLIF and OH* images. The directions of the 12 nozzle orifices are marked by the numbers 1 to 12, in which the odd number and even number show the lower row and upper row orifices, respectively. Only the 6 reaction zones from the lower row of nozzle orifices can be seen. The reaction zone at the three o'clock direction is cut by the laser sheet to visualize the pre-chamber jet from the lower row orifice. The pre-chamber

jet from the upper row orifice is imaged by introducing the laser sheet from the four o'clock direction. This is achieved by rotating the pre-chamber by 30° (one clock angle) while keeping the laser location unchanged.

The number n image of PLIF or OH* is binarized to detect the pre-chamber jet or reaction zone boundary using the threshold of about 10% of the maximum signal intensity. The value at pixel (x, y) inside the pre-chamber jet or reaction zone, $i_{(x,\,y)}$, is assigned to 1. The value of the pixels out of the pre-chamber jet or reaction zone is assigned to 0. The probability distribution index (PDI) at pixel (x, y) is determined by combining all the 90 images from 90 separate cycles using Eq. (5).

$$PDI_{(x,\,y)} = \sum_{n=1}^{90} i_{(x,\,y)}/90 \tag{5}$$

The PDIs of the PLIF or OH* images show the possibility of the pre-chamber jet or reaction zone occurrence. $PDI_{(x,\,y)} = 0$ means no pre-chamber jet or reaction zone at pixel (x, y) in all the 90 images and $PDI_{(x,\,y)} = 1$ means that pre-chamber jet or reaction zone appear at pixel (x, y).
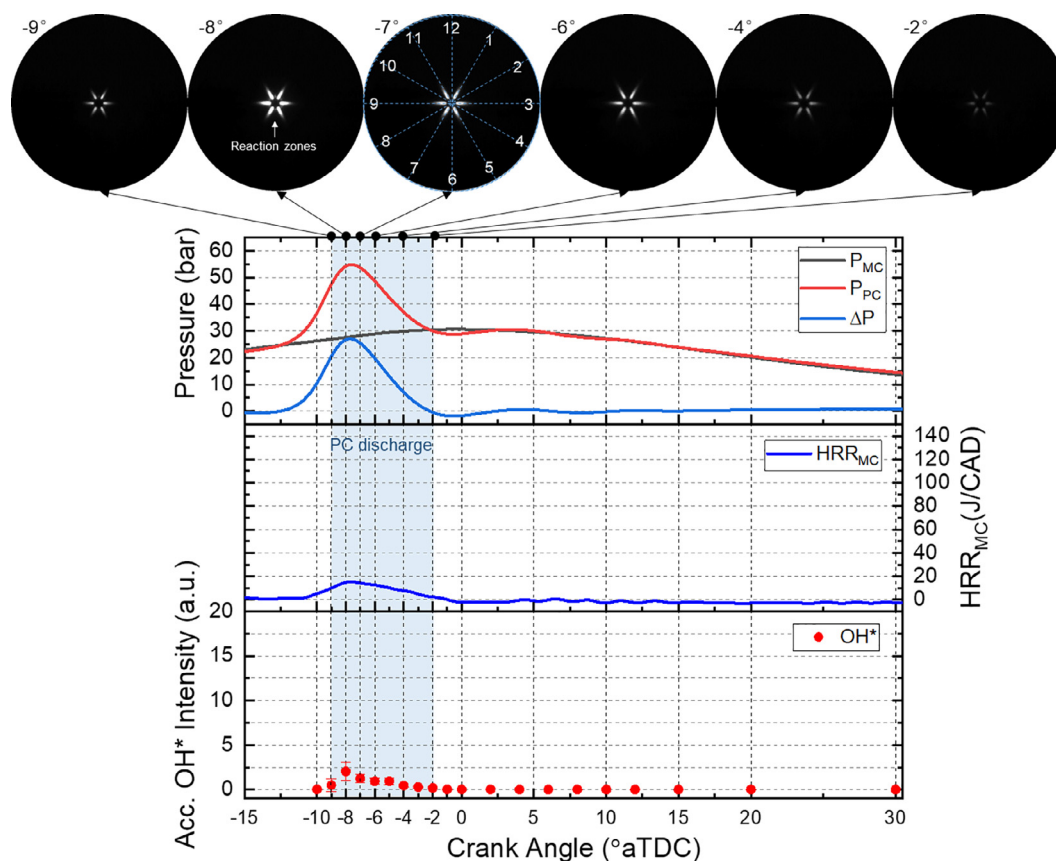
Fig. 5. The combustion process of the unfueled case (PC7.2MC0, λ=11.3). Average pre-chamber (PC), main chamber (MC) pressure, pressure difference between pre-chamber and main chamber (△P), main chamber heat release rate (HRR), and accumulated OH* chemiluminescence intensity. The corresponding averaged OH* images are presented above the chart.

3. Results and discussion

Sections 3.1 and 3.2 compare the PCC combustion characteristics without and with main chamber fueling. The reaction zone and pre-chamber jet evolutions from the lower row orifice of the unfueled, ultra-lean, and lean cases are evaluated and the effects of main chamber fueling on PCC are explored. Section 3.3 compares the jet discharged from the upper row and lower row orifices of the ultra-lean case, highlighting the importance of orifices design to jet penetration and main chamber combustion. Finally, the spatial relationship between the pre-chamber jet and reaction zone is clarified in Section 3.4.

3.1. Reaction zone and pre-chamber jet of the unfueled case (PC7.2MC0, λ=11.3)

Figure 5 shows the pressures, main chamber heat release rate, and the OH* intensity of the unfueled case averaged from 90 cycles. The averaged OH* images at specified crank angles are linked to the evolution of the above parameters. It shows that the main chamber heat release mainly happens during the pre-chamber discharge period shown by the blue rectangle when △P is positive. The accumulated OH* intensity follows the main chamber heat release rate trend well. The timing of peak OH* around −8° corresponds to the timing of the peak of △P. The OH* images only show the reaction zones from the six lower row orifices, marked by the odd numbers shown at −8° No detectable reaction zones appear after −2°

The pressure shows fluctuation after the pre-chamber combustion resulting in both positive and negative △P values. This fluctuation affects the gas exchange between the pre-chamber and main chamber. The mean PLIF and single-shot PLIF images from the lower-row pre-chamber jet of the unfueled case are linked to the mean △P curve in Fig. 6. No jet can be detected before −10 °CA even though the pressure has started to built-up in the pre-chamber. The first jet appears at −9 °CA. The delay between the pressure build-up and the pre-chamber discharge is due to the gas inertia and resistance of the pre-chamber nozzle to the viscous gas inside the pre-chamber. The jet starts to impinge on the piston top after −7° and further penetrates in the main chamber from −7° to −2° The leading part of the jet after impingement shows signs of an anti-clockwise head vortex in the single-shot PLIF images at −4°, −3°, and −2° When the △P becomes negative from −2° and 0°, the jet loses its driving force, but it persists because of gas inertia. The pre-chamber jet appearing from −9° to 0° is named the "main jet" because it takes place during pre-chamber combustion that provides the driving force for the jet. In addition to this main jet, another pre-chamber jet emerges at 8° although the △P at this time is negative. This further proves the aforementioned delay between jet discharge and △P. The jet discharged between 8° and 10° is due to the positive △P between 2° and 6° Similarly, the negative △P between 6° and 10° results in the deceleration and retreat of the jet shown at 12° The jet is more distinct after 15° since the △P becomes positive again due to the volume expansion in the exhaust stroke. Here, we name the pre-chamber jet after 8° as "post jet" to differentiate the "main jet". The post jet is due to the positive △P caused by pressure fluctuation and the cylinder volume expansion.

Comparing the reaction zone in Fig. 5 and the pre-chamber jet in Fig. 6 of the unfueled case, the reaction zone only exists in the main jet period and no reaction zone appears during the post jet period. Although the reaction zone penetration is short
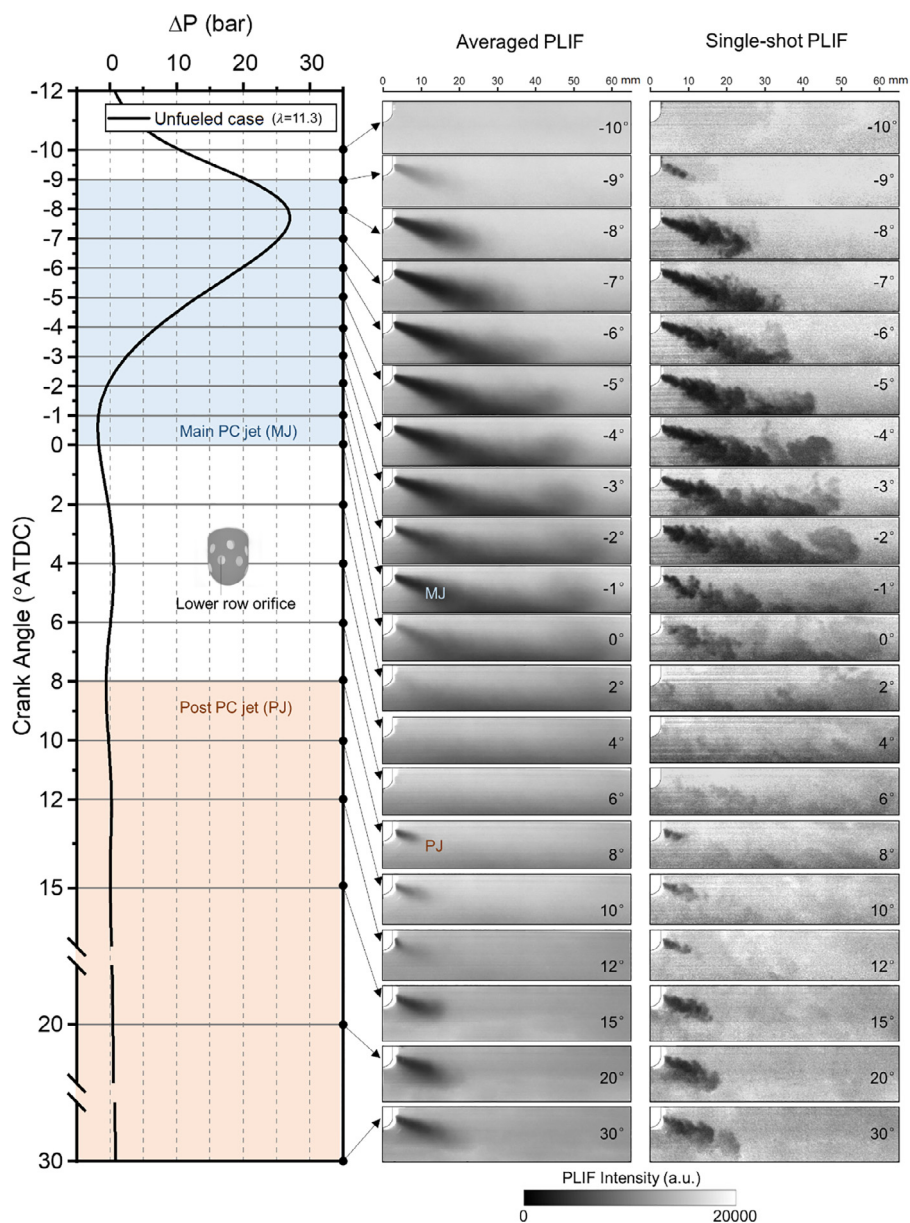
Fig. 6. The pre-chamber jet from the *lower row* orifice of the unfueled case (PC7.2MC0, λ=11.3). Left column: average pressure difference between pre-chamber and main chamber (△P). Middle column: averaged PLIF images. Right column: typical PLIF images. The main jet (MJ) period during pre-chamber combustion and the post jet (PJ) period in the expansion stroke are marked out.

because of no main chamber fueling, the single-shot PLIF image shows that the jet penetrates deep into the region close to the cylinder wall by end of the main jet period at 0° This proves that the low-row pre-chamber orifice design is effective in generating long pre-chamber jet penetration.

### 3.2. Reaction zone and pre-chamber jet when fueling both pre-chamber and main chamber

3.2.1. The ultra-lean case (PC7.2MC54, λ=2.3)

Figure 7 presents the main chamber combustion process of the ultra-lean case. The ignition timing of the pre-chamber charge shown by the rising timing of the △P (−11°) is later than that of the unfueled case (−12°). This should be due to that the pre-chamber charge of the ultra-lean case is enriched (λ<1) by the main chamber fuel entering into the pre-chamber during the compression stroke. Although the peak △P is slightly higher than that of the unfueled case, it shows a much higher main chamber heat

release during the pre-chamber discharge period from −8° to 0°, as shown by the blue rectangle. About 25% of the heat is released during this period. The first OH* image emerges at −8° After that, the reaction zone penetrates fast with a much longer penetration length and it exceeds the field of view by −2° The overall OH* intensity is also much higher, following the main chamber heat release curve well. Again, only the six reaction zones from the lower row orifices are observed. Take the OH* image at −4° for example, the leading part of the reaction zone presents much lower OH* intensity compared to the part closer to the pre-chamber nozzle.

The pre-chamber discharge period finishes after 0° when the △P approaching 0, which is indicated by the fading away of the high OH* intensity in the reaction zone close to the nozzle. The main chamber combustion is dominated by flame propagation. Recall that the global λ of the ultra-lean case is 2.4, which is the lean limit of the stable PCC operation with 1.6 bar fuel MEP in the
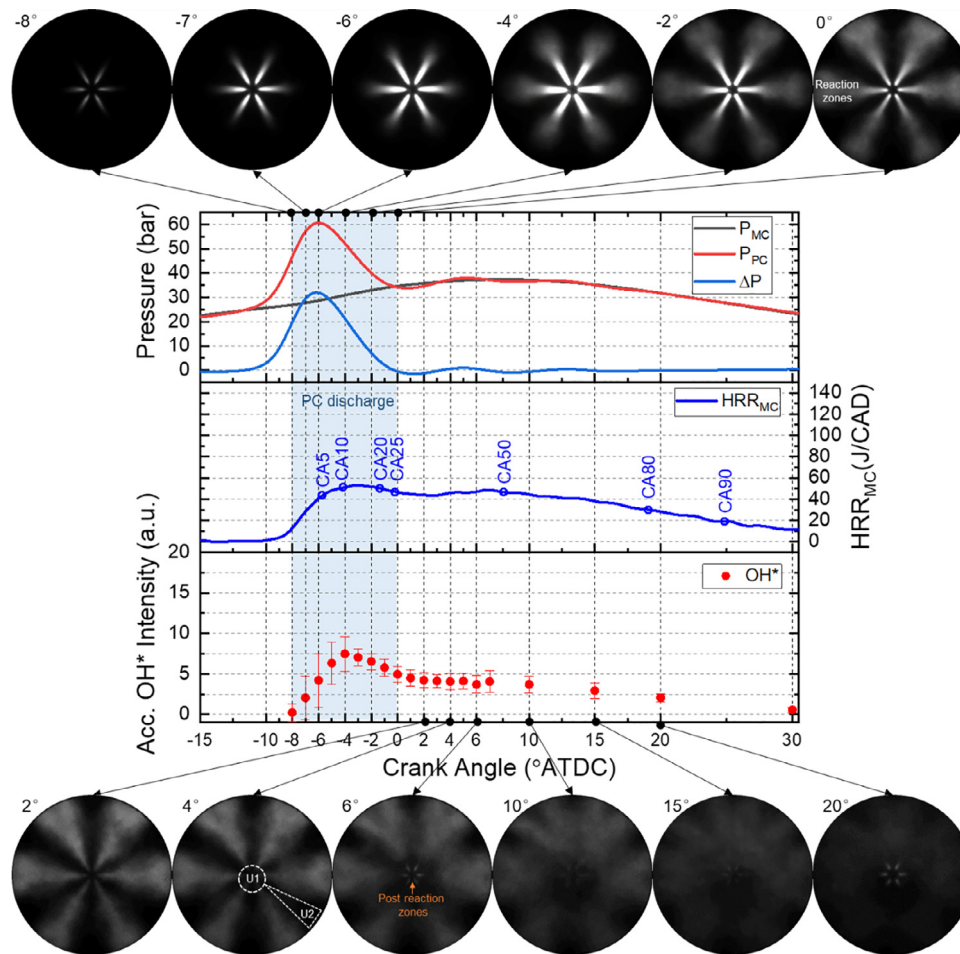
Fig. 7. The combustion process of the ultra-lean case (PC7.2MC54, λ=2.3). Average pre-chamber (PC), main chamber (MC) pressure, pressure difference between pre-chamber and main chamber (△P), main chamber heat release rate (HRR), and accumulated OH* chemiluminescence intensity. The corresponding averaged OH* images in the main chamber are presented above and below the chart. The unburned regions (U1 and U2), and post reaction zones are marked out.

pre-chamber. The OH* images at 2° and 4° shows two unburned regions (U1 and U2) out of the reaction zones. U1 is close to the pre-chamber nozzle shown by the dashed cycle and U2 is between any two adjacent reaction zones shown by the dashed triangle. Note that U2 includes six unburned regions but only one of them is marked out. These two regions could not be fully occupied by flames during the later flame propagation. Note that another reaction zone discharge process is observed after 6° showing much shorter jet penetration length and low OH* intensity. To differentiate the main reaction zone during pre-chamber combustion, we call it "post reaction zone". The post reaction zone is related to the post pre-chamber jet as mentioned in the unfueled case.

Same to the initial reaction zone, the main jet from the low row orifice of the ultra-lean shown in Fig. 8 is first observed at −8° The jet impinges on the piston top one crank angle later. The jet region shown by the PLIF is fully dark because it is accompanied by the reaction zone that consumes the main chamber methane/acetone in the jet region. In comparison, most of the jet region in the unfueled case is not occupied by the flames. Thus, the acetone in the main chamber diffuses into the jet and increases the PLIF signal intensity inside the jet region, as shown in Fig. 6. The jet penetration of the ultra-lean case is faster than that of the unfueled case; the jet reaches the cylinder wall at −3° long before the end of pre-chamber discharge at 1° The reason should be twofold: the higher peak △P provides more driving force to jet discharge and the turbulent combustion of the charge inside the jet enhances the jet boundary expansion.

Similar to the unfueled case, there is a post jet period arising from 6°, which shows a much shorter penetration length compared with the main jet during the pre-chamber combustion. Different from the unfueled case that does not show the post reaction zone, the post jet at 6°, 10°, 20°, and 30° is accompanied by the post reaction zone at the same time in Fig. 7. This post jet period is observed here through negative PLIF imaging thanks to the unburned region close to the pre-chamber nozzle, in which acetone is preserved. The main jets point to the circumferential direction of the cylinder, forming the unburned region (U1) short of turbulence and hot active radicals generated by the pre-chamber discharge, as shown at 6° in Fig. 7. The flame propagation is not sustainable, producing the unburned region around the pre-chamber nozzle after CA90. The other unburned region (U2) between the pre-chamber jets will be discussed in Section 3.3. Comparing the unfueled case that does not show post reaction zone, we know that the post reaction zone shown in the ultra-lean case is due to the enrichment in the pre-chamber charge during the compression stroke.

3.2.2. The lean case (PC7.2MC72, λ=1.8), stable and high-efficient combustion

Figure 9 shows the main chamber combustion process of the lean case. The ignition timing of the pre-chamber combustion is further delayed compared with the ultra-lean case due to pre-chamber charge enrichment by the main chamber fuel. The peak △P is even lower than that of the unfueled case. This indicates
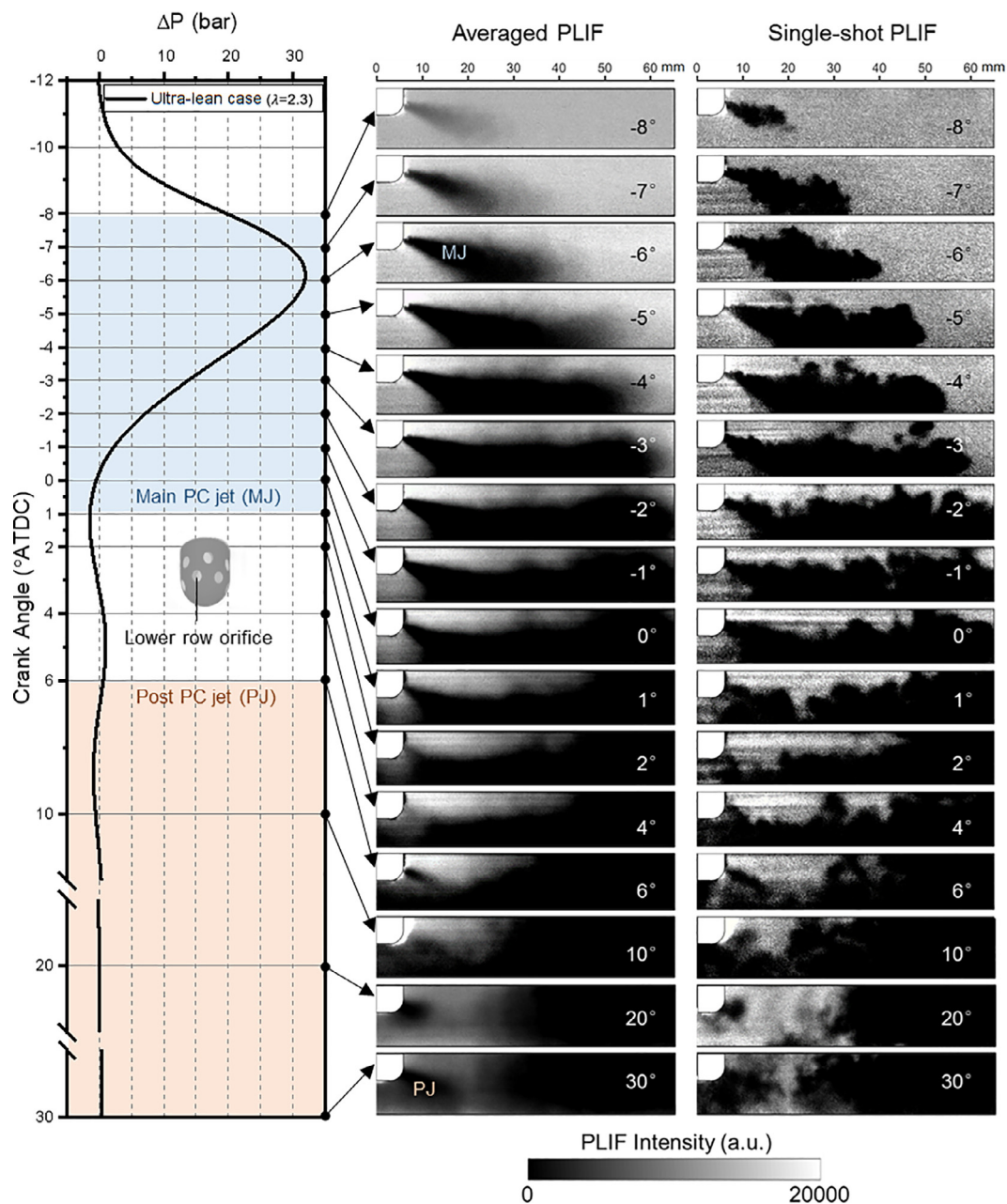
Fig. 8. The pre-chamber jet from the *lower row* orifice and main chamber ignition region of the ultra-lean case (PC7.2MC54, λ=2.3). Left column: average pressure difference between pre-chamber and main chamber (△P). Middle column: averaged PLIF images. Right column: typical PLIF images. The main jet (MJ) period during pre-chamber discharge and the post jet (PJ) period in expansion stroke are marked out.

that the pre-chamber charge of the lean case is over-enriched. The decrease in peak △P will reduce the driving force for the pre-chamber jet discharge. This suggests that it is better to re-duce the fueling of the pre-chamber when the main chamber is richer to avoid this over-enrichment. The lean case presents much higher overall heat release and OH* intensity. The pre-chamber discharge period from −7° to 2° gives about 20% of the overall heat release. The reaction zone is wider than that of the ultra-lean case, making the region between two adjacent reaction zones narrower. Images at −2°, 0°, and 2° show signs of the upper-row reaction zones close to the pre-chamber nozzle and with short penetration length. The typical OH* image at 0° shows that the reaction zone from each lower row orifice is pear-shaped, narrow at the initial part close to the nozzle and wide at the leading part.

After the pre-chamber discharge period, the main chamber combustion is dominated by flame propagation. The flame front propagation at 4° is marked out. The unburned regions of the ultra-lean case shown in Fig. 7 are consumed by the flame propa-gation in the lean case due to the lower global λ. Most of the field of view is occupied by flames at 8° when roughly half of the total heat is released. Note that the post reaction zone shown in the ultra-lean case does not appear in the lean case before 20° This is mainly because the △P is relatively low, resulting in small pressure fluctuation after the pre-chamber combustion; the positive △P that provides the driving force to the pre-chamber charge is not achieved before 20°

Figure 10 shows the lower row pre-chamber jet and main chamber ignition region of the lean case. The jet penetration of the lean case is slower than that of the ultra-lean case; it takes
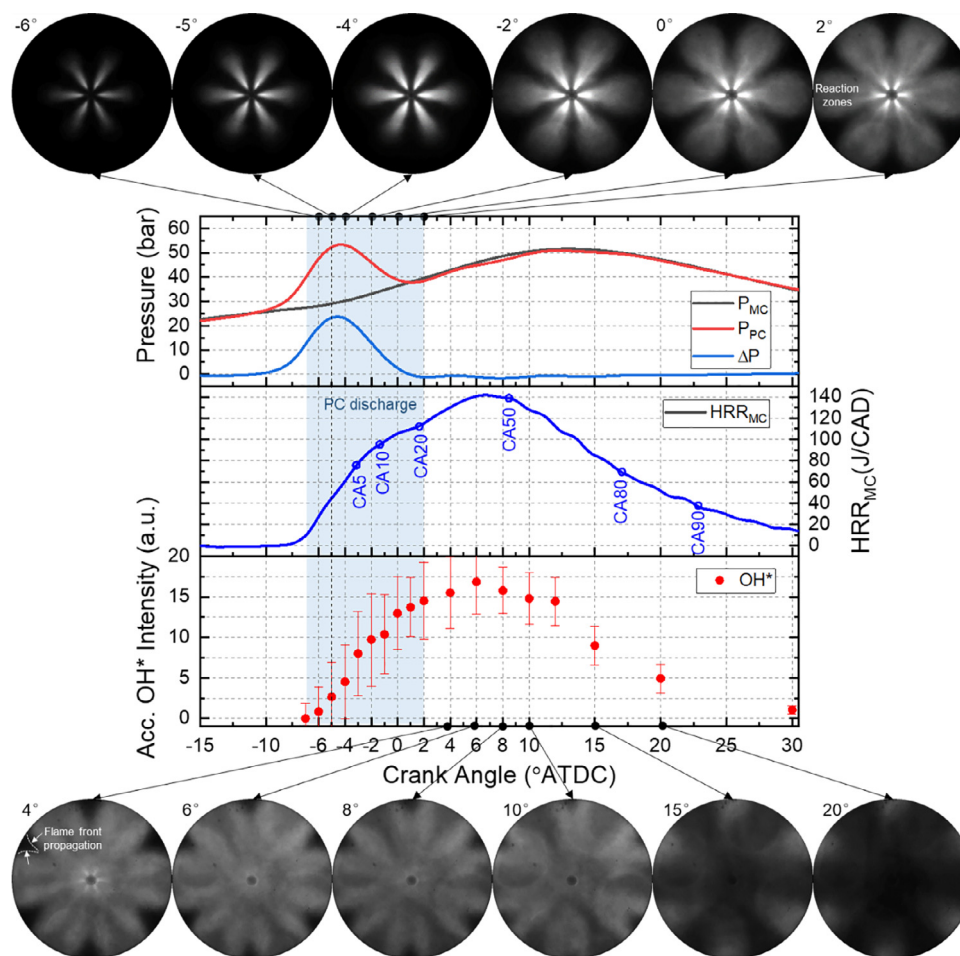
Fig. 9. The combustion process of the lean case (PC7.2MC72, λ=1.8). Average pre-chamber (PC), main chamber (MC) pressure, pressure difference between pre-chamber and main chamber ($\triangle P$), main chamber heat release rate (HRR), and accumulated OH* chemiluminescence intensity. The corresponding averaged OH* images in the main chamber are presented above and below the chart.

about 8° crank angles (from −6° to 2°) for the jet to reach the cylinder wall while it only takes about 5° crank angles in the ultra-lean case. The fuel in the field of view is consumed after 4°, showing negligible PLIF signal intensity. It is interesting to see that the lean case has more complete and stable main chamber combustion but weaker (less momentum and slower jet penetration) pre-chamber jet compared to the ultra-lean case.

The horizontal penetration length and mean horizontal penetration speed of the pre-chamber jet and reaction zone during the pre-chamber discharge are plotted in Fig. 11. The jets from the lower row orifice for all three cases are powerful enough to penetrate to the region near the cylinder wall. The reaction zone of the unfueled case is short and the reaction zone penetration length follows the $\triangle P$ curve trend. The reaction zone penetration length of the ultra-lean and lean cases increases with the pre-chamber jet penetration but is shorter than the jet at the same crank angle.

The mean penetration speed is defined as the rate of change of the mean penetration length. The mean pre-chamber jet speed of all three cases shows a similar trend with $\triangle P$, the maximum of which approximately corresponds to the timing of peak $\triangle P$. The reaction zone penetration speed of the unfueled case is low and becomes negative due to the retreat of the reaction zone after the penetration length decreases. The ultra-lean and lean cases present the same reaction zone penetration speed trend with the jet penetration speed but with relatively lower values when the $\triangle P$ is high; it starts to catch up and exceed the jet penetration speed

when the $\triangle P$ becomes small or negative. It shows that a higher peak $\triangle P$ produces a larger maximum jet penetration speed. The ultra-lean case with the highest peak $\triangle P$ presents the maximum jet speed of about 80 m/s, followed by the unfueled case (about 70 m/s) and the lean case (about 60 m/s). This further proves that the over-enrichment in the pre-chamber charge is not favorable for fast pre-chamber jet discharge.

3.3. Pre-chamber jet comparison between the lower row and upper row orifices of the ultra-lean case

In Sections 3.1 and 3.2, the OH* images do not present distinct reaction zones from the upper row orifices. This implies that the pre-chamber jet of the upper row orifice must be significantly different from that of the lower row shown in Figs. 6,8,10. Figure 12 presents the jet from the upper row orifice of the ultra-lean case. Comparing Figs. 8 and 12, the main jet period (from −8° to 1°) from the upper row orifice is the same as the lower row, but the upper row jet is much weaker with a much shorter penetration length. The umbrella angle of the pre-chamber jet axis (2θ, see PLIF image at −6°) is about 120°, which is smaller than that of the lower row orifice (about 134°). The post jet of the lower row orifice after pre-chamber combustion does not appear during the pressure fluctuation at 6° and 10° Only a very weak post jet around the nozzle appears late after 20° under positive $\triangle P$. Compared with the lower row orifice, the PLIF field of view of the
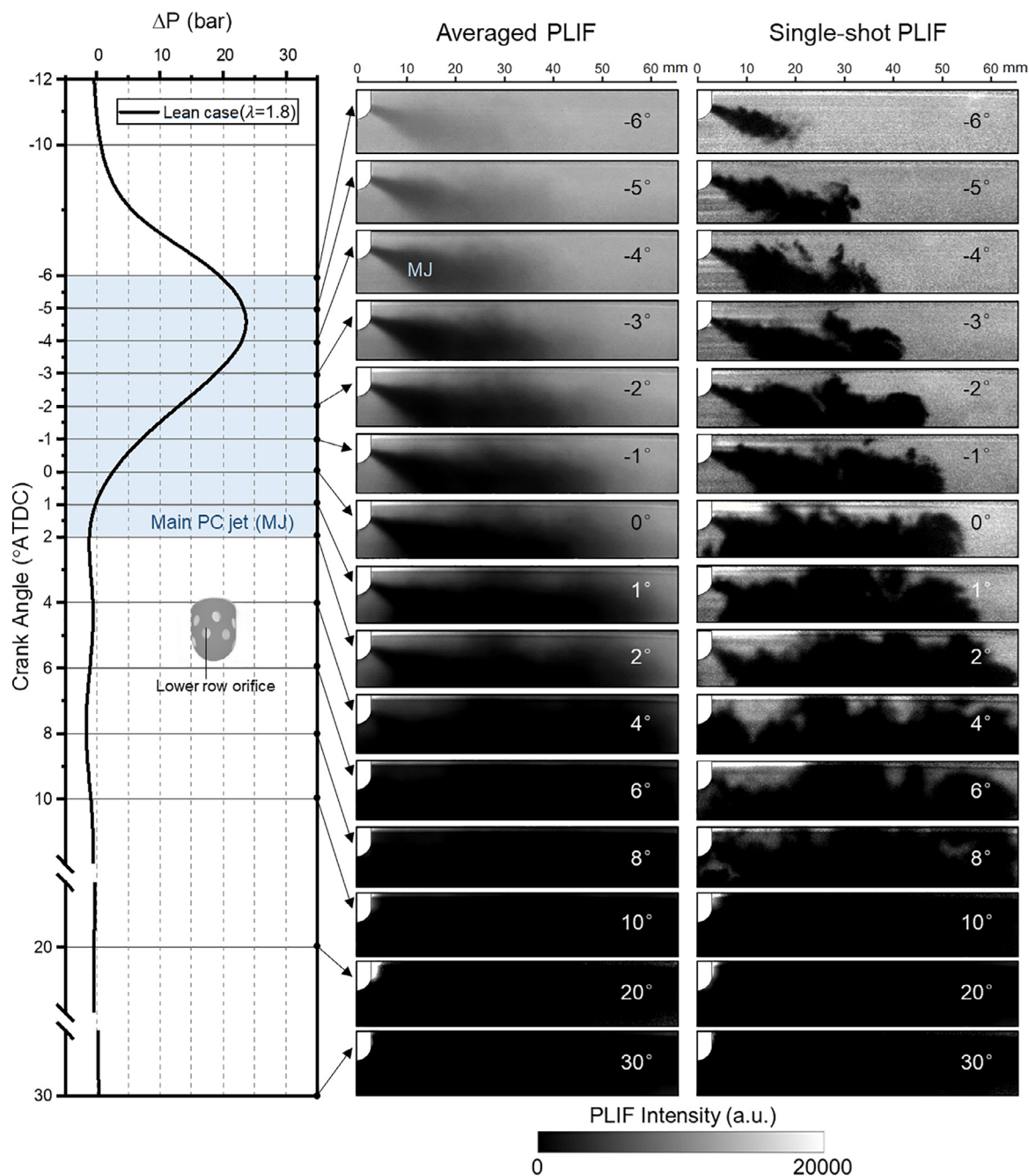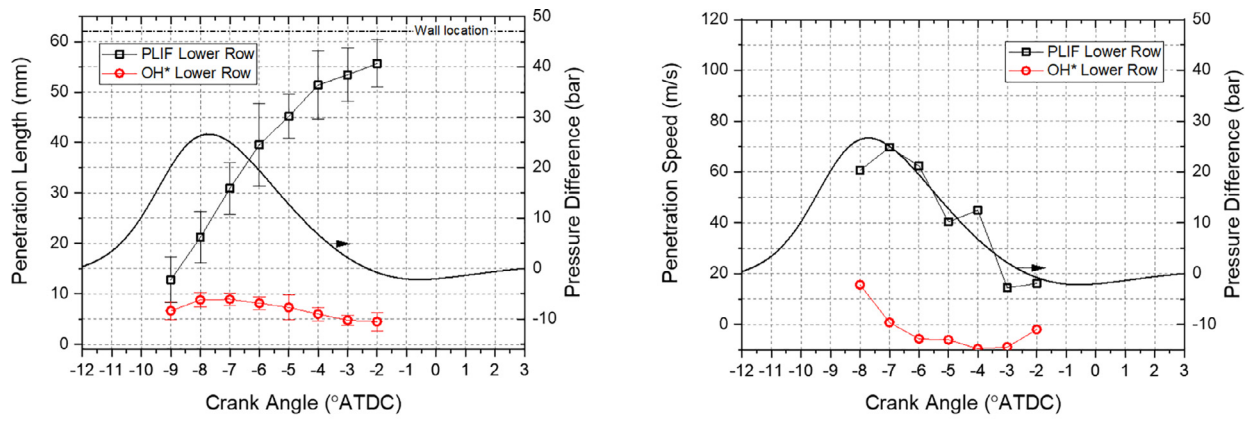
Fig. 10. The pre-chamber jet from the *lower row* orifice and main chamber ignition region of the lean case (PC7.2MC72, λ=1.8). Left column: pressure difference between pre-chamber and main chamber (△P). Middle column: averaged PLIF images. Right column: typical PLIF images. The main pre-chamber jet (MJ) period during pre-chamber discharge is marked out.

upper row orifice presents a much larger unburned region at 30° (after CA90). Note that this field of view corresponds to unburned region U2 marked out in Fig. 7. The unburned region U2 is formed due to the weak pre-chamber jet and thus less active radicals.

Figure 13 shows that the upper row orifice does not present the reaction zone penetration. It seems that the flame is quenched in the upper row orifice due to the low charge flow rate, i.e., the formed over-lean mixture, as indicated in Fig. 12. It also shows that the pre-chamber jet penetration length is much shorter than that of the lower row orifice at the same crank angle, and it could not approach the near-wall region. The mean jet penetration speed follows the same trend of the lower row orifice, peaking at the crank angle around the maximum △P. The peak penetration speed

of about 60 m/s is much smaller than that of the lower row orifice (about 80 m/s).

The observed differences in the pre-chamber jet and reaction zone between the upper and lower row orifices should be due to the pre-chamber nozzle orifice design. As shown in Fig. 2, the included angle for both the upper and lower rows are the same (134°). The upper row orifices are arranged on the straight part of the pre-chamber throat, however, the lower row orifices on the curved surface of the pre-chamber throat tip. When the gas or flame flows downward inside the straight throat during pre-chamber combustion, the lower row orifices have a larger momentum component and thus a higher flow rate of pre-chamber discharge.

(a) Unfueled case (PC7.2MC0, λ=11.3)
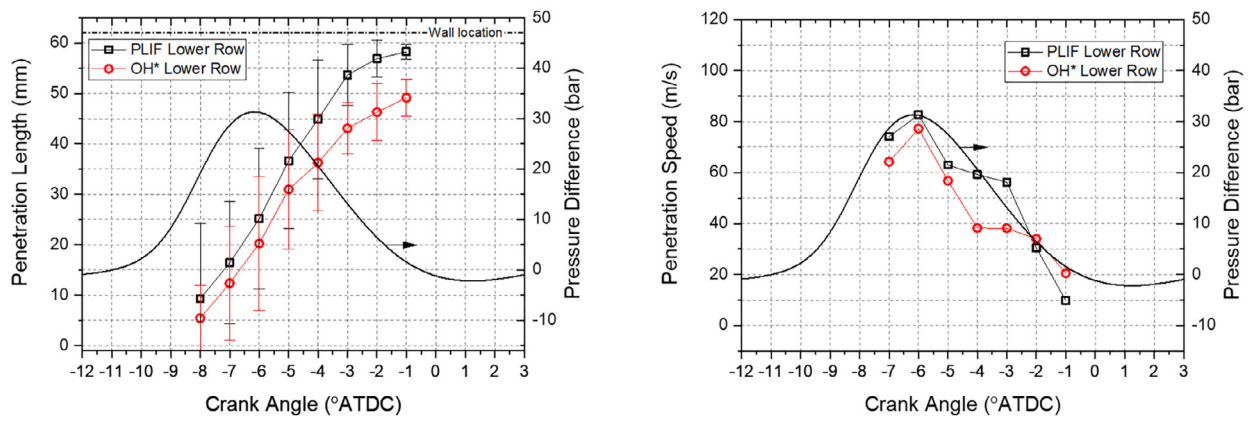
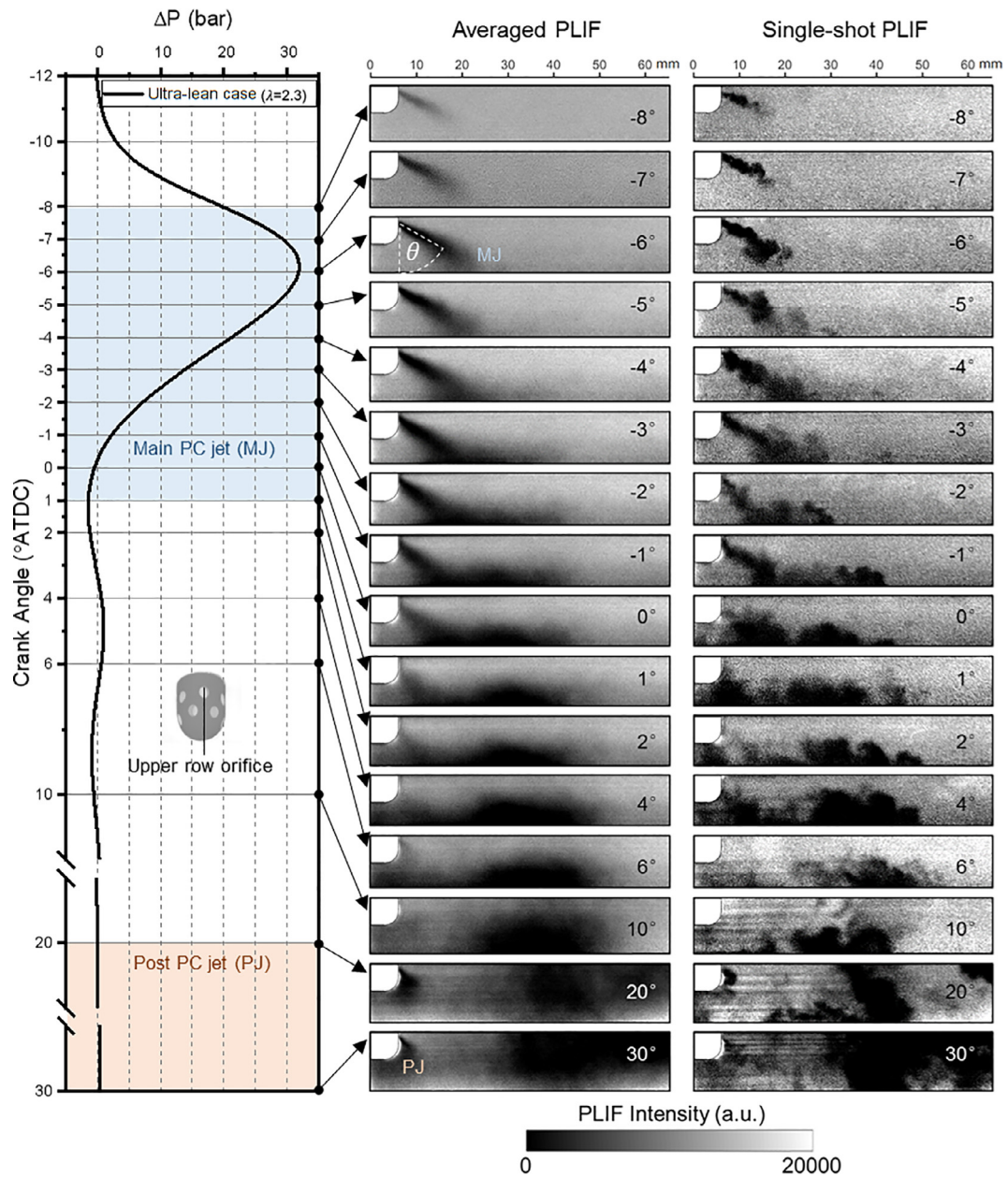(b) Ultra-lean case (PC7.2MC54, λ=2.3)
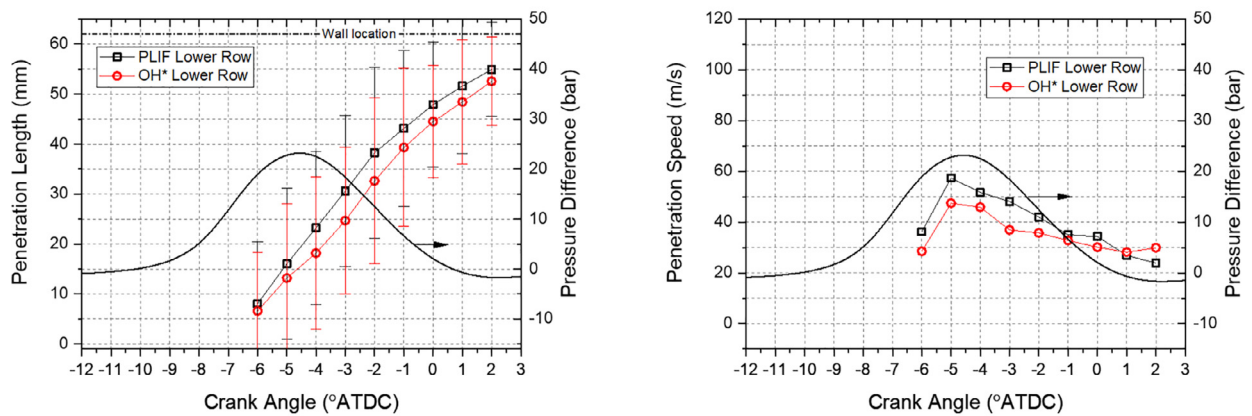
(c) Lean case (PC7.2MC72, λ=1.8)

Fig. 11. The horizontal penetration length and mean horizontal penetration speed of the pre-chamber jet (PLIF) and reaction zone (OH*) from the lower row orifice: the unfueled case (a), the ultra-lean case (b), and the lean case (c).

### 3.4. The spatial relationship between the pre-chamber jet and the reaction zone

Figure 14 clarifies the spatial relationship between the pre-chamber jet and reaction zone for different cases. It shows the probability distribution index (*PDI*) of PLIF and OH* images and simultaneously acquired single-shot PLIF and OH* images at crank angles when the most powerful reaction zone appears ($-8°$ in the

unfueled case, $-4°$ in the ultra-lean case, and $0°$ in the lean case). Note that only the lower row PLIF and OH* images in Fig. 14b are simultaneously acquired. Recall that the *PDI* indicates the occurrence probability of the pre-chamber jet and reaction zone.

The reaction zone becomes wider with higher main chamber fueling; the adjacent reaction zones of the lean case start to merge. Although the OH* signal is line-of-sight, the reaction zone impingement on the piston wall is well reproduced by comparing

Fig. 12. The pre-chamber jet evolution of the *upper row* orifice and main chamber ignition region for the ultra-lean case (PC7.2MC54, λ=2.3). Left column: average pressure difference between pre-chamber and main chamber (△P). Middle column: averaged PLIF images. Right column: typical PLIF images. The main jet (MJ) region during pre-chamber ignition and the post jet (PJ) region in expansion stroke are marked out.
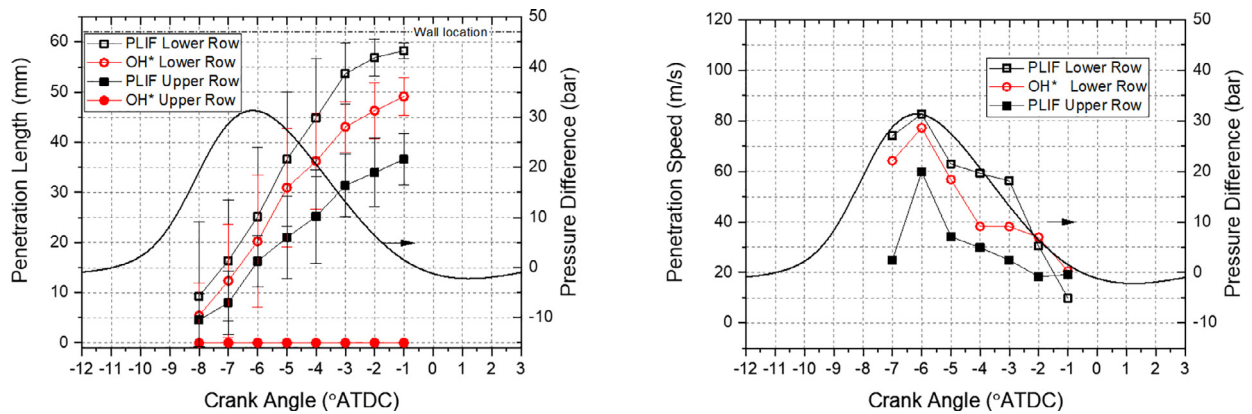
Fig. 13. The horizontal penetration length (a) and mean horizontal penetration speed (b) of the pre-chamber jet (PLIF) and reaction zone (OH*) from the lower row and upper row orifices of the ultra-lean case (λ=2.3).
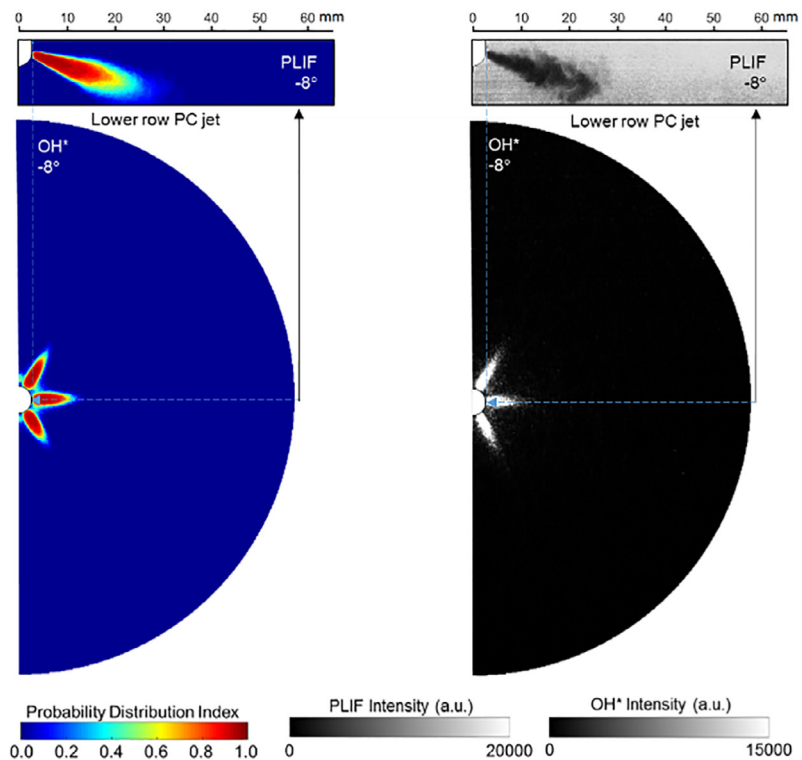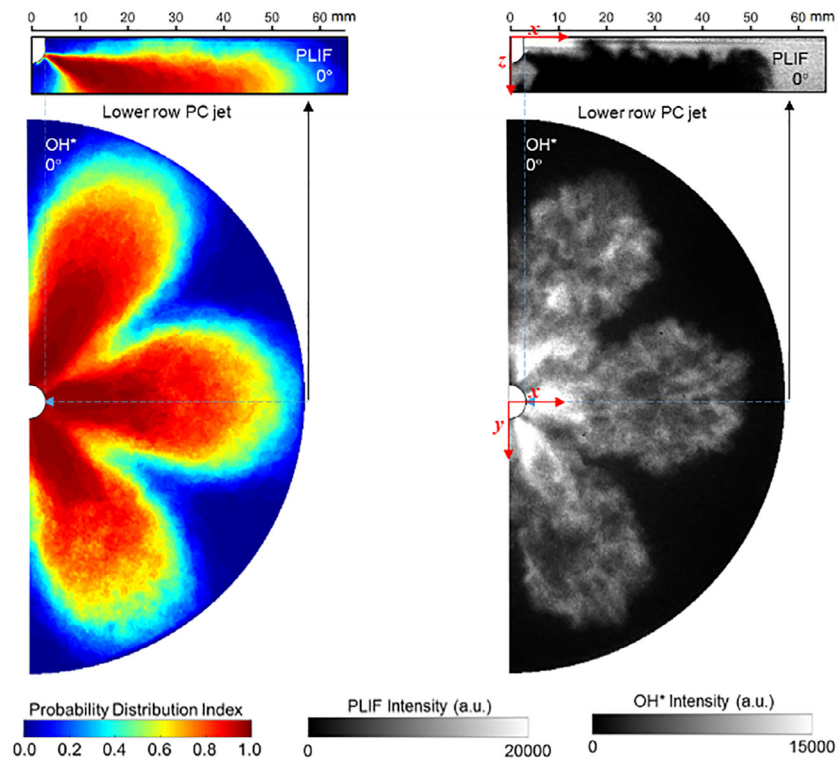
(a) Unfueled case (PC7.2MC0, λ=11.3)
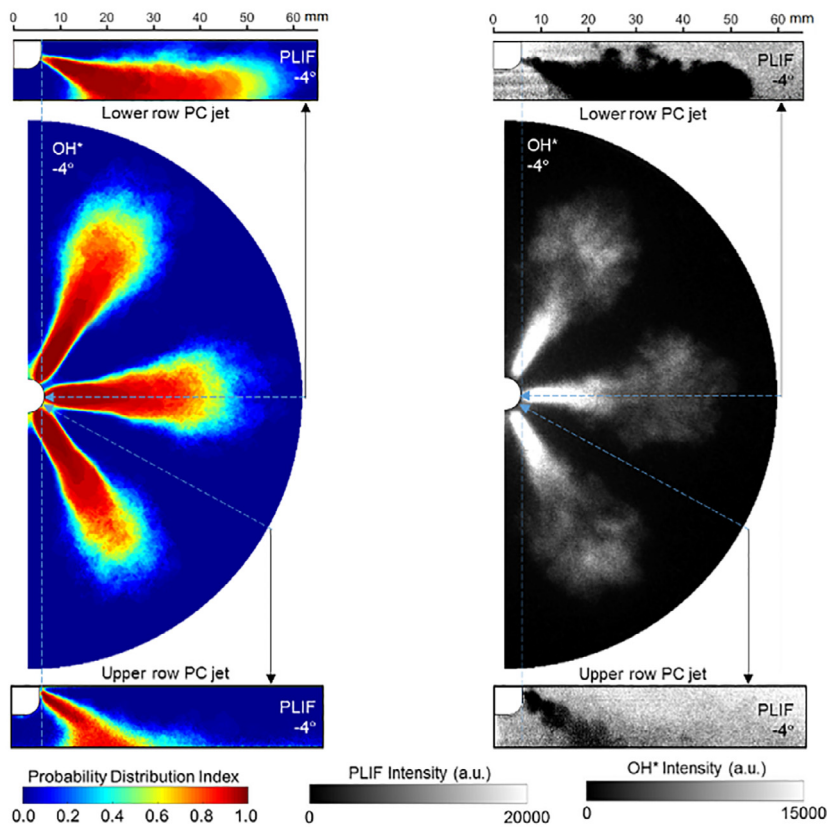
(b) Ultra-lean case (PC7.2MC54, λ=2.3)

Fig. 14. The probability distribution index (*PDI*) and simultaneously acquired, single-shot images of PLIF and OH* at specified crank angles for the unfueled case (a), the ultra-lean case (b), and the lean case (c).

(c) Lean case (PC7.2MC72, λ=1.8)
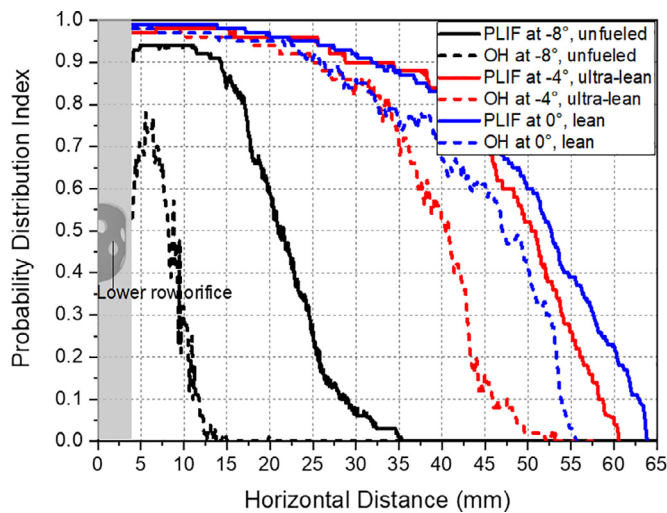
Fig. 14. Continued

Fig. 15. The probability distribution index (*PDI*) along the horizontal direction of the lower row orifice PLIF image and the centreline of the OH* image at −8° in the unfueled case (PC7.2MC0, λ=11.3), at −4° in the ultra-lean case (PC7.2MC54, λ=2.3), and at 0° in the lean case (PC7.2MC72, λ=1.8).

Fig. 16. The horizontal penetration difference (∆L) between pre-chamber jet (PLIF imaging) and reaction zone (OH* imaging) of the unfueled case (PC7.2MC0, λ=11.3), the ultra-lean case (PC7.2MC54, λ=2.3), and the lean case (PC7.2MC72, λ=1.8).

the simultaneously acquired negative PLIF image. In the unfueled case, the reaction zone has a short penetration length and high OH* intensity and *PDI* value. In the ultra-lean and lean cases, the reaction zone far away from the pre-chamber nozzle shows relatively lower OH* intensity and *PDI* value. This trend is also observed in the PLIF imaging that the jet region far away from the nozzle shows a lower *PDI* value. The above features should be mainly due to the leaner charge in the region far away from the main pre-chamber jet; the potential jet-wall impingement and near-wall quenching may also contribute. Figure 15 details the *PDI*
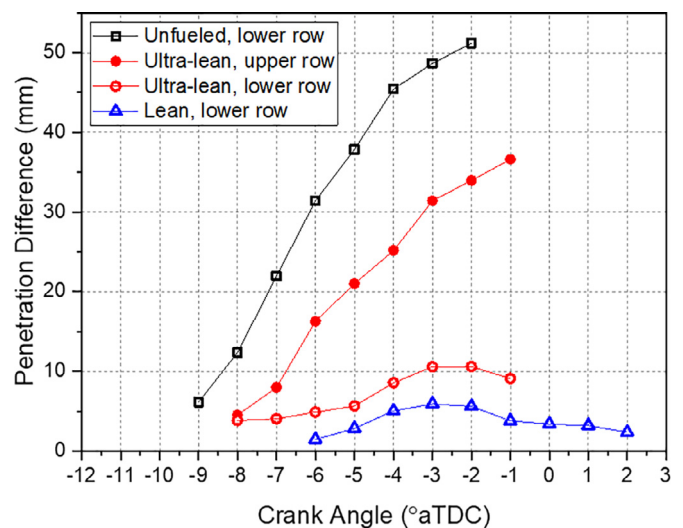
along the centreline (*x*-direction, see Fig. 14c) of the reaction zone and the maximum *PDI* of the pre-chamber jet in the z-direction along the *x*-direction from the low row orifice. It shows that the gap between the pre-chamber jet and reaction zone decrease with higher main chamber fueling.

Figure 16 presents the horizontal penetration difference (∆L) between pre-chamber jet and reaction zone for all the cases. The ∆L from the lower row orifice decreases with higher main chamber fueling. The ∆L for the lower row orifice of the unfueled case and the upper row orifice of the ultra-lean case is much

larger due to the non-fueling of the main chamber (short reaction zone) and the low flow rate of the upper row orifice (no reaction zone), respectively. $\triangle L$ of the lower row orifice of the ultra-lean and lean cases first increases and then decreases, indicating that the reaction zone first lags behind the pre-chamber jet and then catches up as time goes by.

4. Conclusions

We explored the relationship between the pre-chamber jet discharge and main chamber ignition in PCC on an optical engine fueled with methane and equipped with a pre-chamber with two-row orifices. The negative acetone PLIF and OH* chemilu-minescence imaging techniques were applied simultaneously to visualize the pre-chamber jet and reaction zone, respectively. The pre-chamber fueling was constant and the main chamber fueling was increased to generate three cases with different global λ: the unfueled case (λ=11.3), the ultra-lean case (λ=2.3), and the lean case (λ=1.8). The main conclusions are as follows:

The negative acetone PLIF imaging technique can effectively capture the pre-chamber jet discharge process. The jet penetration speed is closely related to the pressure difference between the pre-chamber and main chamber ($\triangle P$); higher $\triangle P$ gives faster jet penetration and the maximum jet penetration speed appears at the timing around the peak $\triangle P$. Over enrichment in the pre-chamber charge reduces the peak $\triangle P$ and thus does not favor a faster pre-chamber jet discharge. The jet characteristics and dynamics can be isolated and better analysed in the unfueled case without interference from the main chamber combustion.

(1) A post jet is visualized in both the unfueled and ultra-lean cases in addition to the main jet. The former is due to the pre-chamber combustion; the latter is due to the $\triangle P$ fluctuation after pre-chamber combustion and the cylinder volume expansion that produces positive $\triangle P$. The simultane-ously acquired PLIF and OH* images show that the post jet is accompanied by the post reaction zone in the ultra-lean case. This proves that the post jet is responsible for the post-combustion of PCC reported in the literature [14].

(2) There are two unburned regions under the lean-limit PCC operating conditions in the ultra-lean case: one is around the pre-chamber nozzle and the other between the adjacent reaction zones. These two unburned regions are consumed by sustainable flame propagation when the main chamber fueling is increased in the lean case. Pre-chamber jet im-pingement on the flat piston wall is witnessed by the PLIF imaging. The region of the pre-chamber jet and reaction zone far away from the nozzle presents a lower probability distribution index.

(3) The jet from the lower-row orifice of the current design is strong enough to penetrate to the region close to the cylinder wall; however, it is not the case for the upper-row orifice. The weak pre-chamber jet from the upper-row orifice does not produce any distinct reaction zone. This indicates that the pre-chamber orifice location and arrange-ment on the nozzle also matters in the pre-chamber design.

(4) The pre-chamber jet penetration length is longer than that of the reaction zone during pre-chamber discharge; the reaction zone first lags behind the pre-chamber jet and then catches up. The overall penetration length difference between the pre-chamber jet and reaction zone decreases with higher main chamber fueling.

Declaration of Competing Interest

None.

Acknowledgments

References

[1] P. Patane, M. Nandgaonkar, Review: multipoint laser ignition system and its applications to IC engines, Optics Laser Technol. (2020) 130.

[2] W.P. Attard, N. Fraser, P. Parsons, E. Toulson, A turbulent jet ignition pre-cham-ber combustion system for large fuel economy improvements in a modern ve-hicle powertrain, SAE Technical Paper 2010-01-1457, 2010.

[3] C.E.C. Alvarez, G.E. Couto, V.R. Roso, A.B. Thiriet, R.M. Valle, A review of prechamber ignition systems as lean combustion technology for SI engines, Appl. Therm. Eng. 128 (2018) 107–120.

[4] E. Toulson, H. Schock, W. Attard, A review of pre-chamber initiated jet ignition combustion systems, SAE Technical Paper 2010-01-2263, 2010.

[5] T. Date, S. Yagi, A. Ishizuya, I. Fujii, Research and Development of the Honda CVCC Engine, SAE International, 1974.

[6] Y. S., O. N., H. T., Ignition and burning process in a divided chamber bomb, Combust. Flame 59 (1985) 11.

[7] L.A. Gussak, V.P. Karpov, Y.V. Tikhonov, The application of lag-process in prechamber engines, SAE Technical Paper 790692, 1979.

[8] W.P. Attard, H. Blaxill, A lean burn gasoline fueled pre-chamber jet ignition combustion system achieving high efficiency and low NOx at part load, SAE Technical Paper 2012-01-1146, 2012.

[9] W.P. Attard, H. Blaxill, A gasoline fueled pre-chamber jet ignition combustion system at unthrottled conditions, SAE Technical Paper 2012-01-0386 5 (2012), pp. 315–329.

[10] W.P. Attard, H. Blaxill, E.K. Anderson, P. Litke, Knock limit extension with a gasoline fueled pre-chamber jet igniter in a modern vehicle powertrain, SAE Technical Paper 2012-01-1143 5 (2012), pp. 1201–1215.

[11] W.P. Attard, P. Parsons, Flame kernel development for a spark initiated pre-chamber combustion system capable of high load, high efficiency and near zero NOx emissions, SAE Technical Paper 2010-01-2260, 2010.

[12] A. Shah, P. Tunestal, B. Johansson, Effect of relative mixture strength on perfor-mance of divided chamber 'avalanche activated combustion' ignition technique in a heavy duty natural gas engine, SAE Technical Paper 2014-01-1327, 2014.

[13] A. Shah, P. Tunestal, B. Johansson, Effect of pre-chamber volume and nozzle di-ameter on pre-chamber ignition in heavy duty natural gas engines, SAE Tech-nical Paper 2015-01-0867, 2015.

[14] P. Hlaing, M. Echeverri Marquez, E. Singh, F. Almatrafi, E. Cenker, M. Ben Houidi, B. Johansson, Effect of pre-chamber enrichment on lean burn pre-chamber spark ignition combustion concept with a narrow-throat geom-etry, SAE Technical Paper 2020-01-0825, 2020.

[15] P. Hlaing, M. Echeverri Marquez, V.S. Bhavani Shankar, E. Cenker, M. Ben Houidi, B. Johansson, A study of lean burn pre-chamber concept in a heavy duty engine, SAE Technical Paper 2019-24-0107, 2019.

[16] S. Biswas, S. Tanvir, H. Wang, L. Qiao, On ignition mechanisms of premixed CH 4 /air and H 2 /air using a hot turbulent jet generated by pre-chamber combustion, Appl. Therm. Eng. 106 (2016) 925–937.

[17] S. Biswas, L. Qiao, Ignition of ultra-lean premixed H2/air using multiple hot turbulent jets generated by pre-chamber combustion, Appl. Therm. Eng. 132 (2018) 102–114.

[18] S. Biswas, L. Qiao, Ignition of ultra-lean premixed hydrogen/air by an imping-ing hot jet, Appl. Energ. 228 (2018) 954–964.

[19] E. Mastorakos, P. Allison, A. Giusti, P. De Oliveira, S. Benekos, Y. Wright, C. Frouzakis, K. Boulouchos, Fundamental aspects of jet ignition for natural gas engines, SAE Int. J. Eng. 10 (2017) 2429–2438.

[20] P.M. Allison, M. de Oliveira, A. Giusti, E. Mastorakos, Pre-chamber ignition mechanism: experiments and simulations on turbulent jet flame structure, Fuel 230 (2018) 274–281.

[21] G. Gentz, B. Thelen, M. Gholamisheeri, P. Litke, A. Brown, J. Hoke, E. Toulson, A study of the influence of orifice diameter on a turbulent jet ignition system through combustion visualization and performance characterization in a rapid compression machine, Appl. Therm. Eng. 81 (2015) 399–411.

[22] G. Gentz, M. Gholamisheeri, E. Toulson, A study of a turbulent jet ignition sys-tem fueled with iso-octane: pressure trace analysis and combustion visualiza-tion, Appl. Energ. 189 (2017) 385–394.

[23] M. Gholamisheeri, B.C. Thelen, G.R. Gentz, I.S. Wichman, E. Toulson, Rapid compression machine study of a premixed, variable inlet density and flow rate, confined turbulent jet, Combust. Flame 169 (2016) 321–332.

[24] M. Gholamisheeri, I.S. Wichman, E. Toulson, A study of the turbulent jet flow field in a methane fueled turbulent jet ignition (TJI) system, Combust. Flame 183 (2017) 194–206.

[25] Y. Kawabata, D. Mori, Combustion diagnostics and improvement of a precham- ber lean-burn natural gas engine, SAE Technical Paper 2004-01-0979, 2004.

[26] E. Toulson, A. Huisjen, X. Chen, C. Squibb, G. Zhu, H. Schock, W.P. Attard, Visu- alization of propane and natural gas spark ignition and turbulent jet ignition combustion, SAE Int. J. Eng. 5 (2012) 1821–1835.

[27] W.P. Attard, E. Toulson, A. Huisjen, X. Chen, G. Zhu, H. Schock, Spark ignition and pre-chamber turbulent jet ignition combustion visualization, SAE Techni- cal Paper 2012-01-0823, 2012.

[28] M. Bunce, H. Blaxill, W. Kulatilaka, N. Jiang, The effects of turbulent jet charac- teristics on engine performance using a pre-chamber combustor, SAE Technical Paper 2014-01-1195, 2014.

[29] J. Duong, R. Wellander, J. Hyvönen, Ö. Andersson, M. Richter, B. Johansson, M. Álden, High speed combustion imaging in a large bore gas engine-the re- lationship between pre and main chamber heat release, Proceedings of the ASME 2013 International Mechanical Engineering Congress and Exposition, San Diego, California, USA (2013).

[30] B. Korb, K. Kuppa, H.D. Nguyen, F. Dinkelacker, G. Wachtmeister, Experimental and numerical investigations of charge motion and combustion in lean-burn natural gas engines, Combust. Flame 212 (2020) 309–322.

[31] M. Echeverri Marquez, P. Hlaing, Q. Tang, R. Sampath, E. Cenker, M. Ben Houidi, G. Magnotti, B. Johansson, High-Speed Imaging of Main-Chamber Combustion of a Narrow Throat Pre-Chamber Under Lean Conditions, SAE Technical Paper 2020-01-2081, 2020.

[32] R. Wellander, J. Rosell, M. Richter, M. Alden, O. Andersson, B. Johansson, J. Duong, J. Hyvonen, Study of the early flame development in a spark-ignited lean burn four-stroke large bore gas engine by fuel tracer PLIF, SAE Int. J. Eng. 7 (2014) 928–936.

[33] Q. Tang, R. Sampath, M. Echeverri Marquez, P. Hlaing, P. Sharma, M. Ben Houidi, E. Cenker, J. Chang, G. Magnotti, B. Johansson, Simultaneous Negative PLIF and OH* Chemiluminescence Imaging of the Gas Exchange and Flame Jet from a Narrow Throat Pre-Chamber, SAE Technical Paper 2020-01-2080, 2020.

[34] R. Sampath, Q. Tang, M. Echeverri Marquez, P. Sharma, P. Hlaing, M. Ben Houidi, E. Cenker, J. Chang, B. Johansson, G. Magnotti, Study On the Pre-Cham- ber Fueling Ratio Effect On the Main Chamber Combustion Using Simultaneous PLIF and OH* Imaging, SAE International, 2020.

[35] Q. Tang, R. Sampath, P. Sharma, G. Nyrenstedt, A. Al Ramadan, M. Ben Houidi, J. Badra, B. Johansson, G. Magnotti, SAE Technical Paper Series, SAE Technical Paper 2020-01-1192, 2020.

[36] Q. Tang, Y. An, V. Raman, H. Shi, J. Sim, J. Chang, G. Magnotti, B. Johansson, Ex- perimental study on the effects of spray–wall interaction on partially premixed combustion and engine emissions, Energ. Fuel 33 (2019) 5673–5681.